Combined Current and Temperature Mapping in an Air-Cooled, Open-Cathode Polymer Electrolyte Fuel Cell Under Steady-State and Dynamic Conditions.

Q. Meyer[1], K. Ronaszegi[1], J.B. Robinson[1], M. Noorkami[1], O. Curnick[2], S. Ashton[2], A. Danelyan[2], T. Reisch[2], P. Adcock[2], R. Kraume[3], P. R. Shearing[1], D. J. L. Brett[1]*

[1] Electrochemical Innovation Lab, Department of Chemical Engineering, UCL, London, WC1E 7JE, United Kingdom

[2] Intelligent Energy, Charnwood Building Holywell Park, Ashby Road, Loughborough Leicestershire, LE11 3GB, United Kingdom

[3] S^{++} Simulation Services, Waldstraße 5, 82418 Murnau-Westried, Germany

* Author to whom correspondence should be addressed

Tel.: +44(0)20 7679 3310

Web: www.ucl.ac.uk/electrochemical-innovation-lab

Email: d.brett@ucl.ac.uk

Abstract

In situ diagnostic techniques provide a means of understanding the internal workings of fuel cells so that improved designs and operating regimes can be identified. Here, for the first time, a combined current density and temperature distributed measurement system is used to generate an electro-thermal performance map of an air-cooled, air-breathing polymer electrolyte fuel cell stack operating in an air / hydrogen cross-flow configuration. Analysis is performed in low- and high-current regimes and a complex relationship between localised current density, temperature and reactant supply is identified that describes the way in which the system enters limiting performance conditions. Spatiotemporal analysis was carried out to characterise transient operations in dead-ended anode / purge mode which revealed extensive current density and temperature gradients.

Keywords

Current mapping; temperature mapping; air-breathing fuel cell; performance optimisation; spatiotemporal electro-thermal analysis.

1. Introduction

Polymer electrolyte fuel cells (PEFCs) are complex devices, due to the variety of operational strategies (liquid/air cooled, humidified/dry gases), designs (closed/open cathode, through-flow/dead-ended) and materials. Understanding of the *in-situ* behaviour and more specifically of the complex interaction between localised current and temperature is crucial for the development of improved systems.

Current mapping was first introduced by Cleghorn and Derouin[1] and Brett *et al.* [2,3], using printed circuit board (PCB) technology to produce segmented current collector plates, along with Stumper *et al.*[4], using segmented membranes. This technique shows that significant current density gradients can be generated as a result of fuel and oxidant depletion. Other techniques have proven the value of localised current measurements, including segmented PCBs [1,3,5–9], segmented current collector plates [10–12], shunt resistors [13–15] and Hall effect sensors [16–21]. Measurements have also been performed at sub-millimetre resolution [22,23], investigating the gradients across the land and channel areas. Most studies highlighted uneven performance under high current density, uneven fuel consumptions [2,5,6,14], the crucial influence of the operating conditions [3,13,19], stoichiometric ratios [8,11,12,20], fuel orientations [6,13], water management [10], CO electro-oxidation [7] and CO poisoning [24,25] distribution.

Temperature distribution has also been extensively studied, identifying areas of higher electrochemical activity, hot spot formation and fuel depletion. Thermocouples can provide a crude measure of temperature inside fuel cells [16,17,26,27] but have accuracy limited to $\pm 1^{o}C$ and cannot provide high spatial resolution. Moreover, thermocouples need to be inserted inside the fuel cell, which often requires design modifications. In contrast, infrared thermal imaging can provide very high spatial and temperature resolution [28–34], yet it typically requires use of specially designed fuel cells with a window transparent to infrared radiation, or is otherwise confined to measurement of the outer surface of a cell or stack.

Although current density and temperature have been separately investigated, little has been reported on the combined current and temperature mapping of PEFCs. Studies have used micro-thermocouples arrays inserted within a cell [17,35] and infrared transparent windows [15,30] for temperature measurement; current density measurements performed using PCB segment plates. In the case of the thermocouple insertion method [17,35], they have to be positioned between the cathode flow field and the membrane electrode assembly (MEA) to provide accurate reading, which could affect the flow of reactants and access to the electrodes; similarly, the introduction of the window [15,30] might alter the water condensation, and overall thermal management aspects of cell performance.

Comprehensive understanding of temperature and current density distribution is essential for effective design of PEFCs to assess steady-state operation over a range of operating conditions / modes. For air-cooled open-cathode systems, in which a stream of air generated by external fans concurrently services both the cooling requirement of the stack and supply of oxygen to the cathode, the need to understand the link between electrochemical and thermal performance is particularly important. The electro-thermal performance of such systems has been investigated previously at a whole-stack level[36], but methods of spatiotemporal electro-thermal analysis are required.

Knowledge of the temperature and current density distribution is also essential for understanding transient processes occurring in PEFCs operated in dead-ended mode. During the voltage decay observed in dead-ended mode [37–41], multiple processes are have been identified to play a part, including water accumulation

(highlighted using neutron imaging [37,38]) and nitrogen accumulation (measured via off-gas analysis [37,42,43]).

Meyer *et al*. [37] reported an increase of the overall temperature and ohmic resistance in dead-ended mode. Eventually, local current density could be much higher than the average, and the overall effect could be a local drying of the membrane due to the enhanced reaction heat. Therefore, understanding of the spatiotemporal evolution of the electro-thermal map at constant load but in dead-ended mode would be useful to investigate these claims.

Here, we present the results obtained using a PCB sensor plate device that incorporates both current collection and temperature measurement in close registration with each other. The technique is applied to an air-cooled PEFC where the plate is inserted at the middle of a 5-cell stack. Both steady-state and dynamic operation are investigated.

2. Experimental

Fuel cell testing - A 5-cell (60 cm^2 active area) air-cooled fuel cell stack was used for testing (Intelligent Energy Ltd., UK). The membrane electrode assembly was composed of commercially available gas diffusion layers and commercially available state-of-the art membrane with Pt loading of 0.1 and 0.4 mg cm^{-2} on the anode and cathode, respectively.

The fuel cell test station supplied dry, non-heated, hydrogen (with a purity of 99.995 %) into the anodes and air was blown by three fans (SanAce 36, Sanyo Denki) to the

open-cathode channels. The exhaust hydrogen flow rate in through-flow mode was measured using a thermal mass flow meter (MassVIEW, Bronkhorst) to be 4.7 SLPM (standard litres per minute) when no load was applied. The fans, which provide cooling and air supply to the cathode, were controlled by a programmable power supply (3649A Agilent). The current drawn from the PEFC was controlled by an electronic load (6060B, Agilent) in galvanostatic mode. An in-house computer controlled system coordinates the air, hydrogen, cooling and electrical valves (LabVIEW, National Instruments) as well as recording and presenting data using a data acquisition card (PCI 6221, National Instruments). Ambient temperature, pressure (absolute) and relative humidity (RH) were measured, being of around 25 °C, 1.02 bar (Abs) and 40% RH respectively, during all tests. The operation of this fuel cell in terms of cathode design, cooling and active channels[36], temperature uncertainty [44] and water management in dead-ended anode mode [37] has been described in previous work.

Surface temperature mapping: Thermal imaging was performed using a 640×512 focal plane array camera (SC5600MB FLIR, UK). The images were recorded using commercially available software (ResearchIR, FLIR ATC, Croissy-Beaubourg, France). The camera has an extended wavelength detector allowing detection of infrared light within the range 2.5 μm - 7 μm. The cavity nature of the cooling and active channels approximate to quasi-blackbody emitters, with an emissivity of 1. The thermal camera used during the experiments has a noise equivalent temperature difference (NETD), a measure of the signal-to-noise ratio, of approximately 19 mK which is within the range of calibration required for the

accurate measurement of absolute temperatures. The geometry of the systems imaged resulted in a pixel resolution of approximately 27 µm across the image.

Combined current and temperature mapping: A device for the measurement of the current and temperature distribution, based on PCB technology, was developed by S++ (S++ Simulation Services, Germany). The device is shown in Fig.2 a. The temperature measurement is made with copper 'meanders'. Copper has a temperature coefficient of resistance of 3.9×10^{-3} K^{-1}. The copper wires are supplied with a constant current of 2 mA and the voltage drop across each wire is measured, with its changes proportional to the temperature variations. Current measurement is made with integrated shunt resistors, using a special alloy with a much lower temperature coefficient than copper, therefore relatively insensitive to temperature changes. The resistance of an individual shunt resistor is ≈ 4 mΩ. The shunt resistors and copper 'meanders' are integrated into a printed circuit board (PCB) with gold plated contact segments. Each rectangular contact segment, reading one current and covering one copper meander has an area of 3.75 cm^2. The 16 segments (Fig. 1 a) combined cover the total membrane active area. A multiplexer successively scans the 16 segments and sends the signal to an amplifier and analog-to-digital converter (Fig. 1 b). Finally, the signal is sent to the computer via a USB interface. After calibration, the actual current density and temperature profile is obtained. The fuel cell is operated in galvanostatic mode, and since isopotential conditions are assumed, an applied total current provides a constant voltage through the plate and a distribution of local current density.

Insertion of the sensor plate into the fuel cell: The sensor plate is integrated between an anode and a cathode plate, in the centre of the fuel cell stack. The air flows through the active and cooling channels (Fig. 1 c) of the stack.

The sensor plate captures the local temperature and current density from the air inlet, from Segments 1, 2, 3, 4, to the air exhaust in Segments 13, 14, 15, 16, and the hydrogen inlet, Segments 1, 5, 9, 13 to hydrogen outlet, Segments 4, 8, 12, 16, as displayed Fig. 2. This flow orientation was be used throughout the work, unless stated otherwise.

3. Results and Discussion

In characterising the electro-thermal performance of the stack, the external temperature distribution is first described using infrared thermal imaging. Then the link between internal temperature and current density distribution is considered under steady-state conditions. Finally, the spatiotemporal electro-thermal performance is examined for dead-ended / purge anode transients.

3.1. Thermal imaging of external stack temperature

The influence of temperature on the performance of air-cooled open-cathode fuel cells has been reported previously using thermal imaging and thermocouples [36,37,44]. However, thermal imaging only gives an indication of the external temperature of the stack and thermocouples are normally limited to a few single-point measurements.

However, when used in combination with an array of internal temperature measurements, thermal imaging provides a useful external boundary condition with very high spatial resolution. By changing the fans' orientations, (either blowing air or aspirating air through the stack), it is possible the capture the temperature of the air inlet or the air outlet.

Fig. 3(a) describes the temperature range and distribution observed on the air inlet and outlet of the stack operating over a range of average current densities. Little influence of the fans' orientations is seen on the voltage response.

The temperature distribution over the x-axis, for the air inlet and air exhaust, is depicted using bars centred at the average temperature in Fig. 5(a). The temperature span is quite significant over the x-axis and increases with higher current densities up to 17 ^{o}C at 0.92 A cm^{-2}. It also significantly increases over the y-axis, with a temperature span reaching 30 ^{o}C at limiting current density.

Thermograms in Fig. 2 (b) reveal hot spots towards the hydrogen inlet (left) of the stack, however, the ability to determine the cause of this localised heating effect is limited. Thermal imaging only provides the surface temperature; in order to obtain the heat profile inside the stack, and associate this with current density distribution, a combined internal current and temperature mapping approach is required. Here, such an approach is taken to study steady-state performance in cross-flow configuration and in dynamic mode to investigate dead-end / purge operation.

3.2. Current and temperature mapping

Combined current and temperature distribution mapping was performed in two regimes of operation based on 'low' (<0.46 A cm^{-2}) and 'high' average current density (0.46 to 0.93 A cm^{-2}).

3.2.1. Current and temperature mapping in the low current density regime.

Considering the current density distribution (Fig.4 a and b), one can see that the segments exhibit a gradient along the x-axis (hydrogen flow direction), with decreasing current density the further away from the hydrogen inlet. This is consistent with the consumption, and depletion, of hydrogen, even though the hydrogen has a stoichiometry of λ_{H2} = 4. The oxygen stoichiometry, based on a constant air flow rate, generated by the fans through the tests (details on the calculations can be found in previous work[36]) is of 40 at 0.46 A cm^{-2}. In the y-axis (air flow direction) it can be seen that there is a change in direction of gradient at the start and end of the cell. The columns on the left (at the hydrogen inlet) actually increase in current, whereas those at the hydrogen exit decrease in the air flow direction.

The temperature increases approximately linearly with increasing current density in every segment (Fig.4 c). Although the current density is similar in the first and second column, the first column remains slightly colder because it is fed with hydrogen at ambient temperature, which acts to cool the entrance to the stack. The current density gradient creates a temperature gradient along the x-axis, as a lower current density reduces heat generation (Fig.4 c-d).

The highest temperature is observed around Segments 9, 10, 13, 14 due to the proximity to the hydrogen inlet and air exhaust, this is consistent with the thermal

imaging observations at 0.46 A cm^{-2}, showing the appearance of a hot spot between the first and second quadrant (Fig. 3 b).

This is an example of the coupled effect of current and temperature. The higher temperature at the hydrogen inlet produces a better performance environment with higher electrolyte conductivity, actually leading to improved performance despite the cathode suffering from uneven cooling. Segments 3 and 4 have low temperature and current density, due to the low hydrogen efficiency and proximity to air inlet.

3.2.2. Current and temperature mapping in the high current density regime

Above 0.8 A cm^{-2}, a redistribution of the current distribution profile is observed (Fig. 5 a-b), with substantial current density gradients occurring in both the x- and y-axis. The temperature of most segments (Fig. 5 c-d) increases in an exponential fashion, as a result of the increase in current density.

To focus on performance at high current, Fig. 6 compares segments located at extreme locations of the cell. The current density of Segments 10 and 14, representing the high temperature region, shows that the rate of current increase is tapered, whereas that of Segments 3 and 4, the low temperature region, increases more rapidly with increasing load (Fig. 6 a).

The high temperature region is in excess of 70°C in Segments 13 and 14 (Fig. 6 b); given the very high flow rate and un-humidified air stream, the membrane resistance is likely to increase due to dehydration under these conditions [45–47]. This is a high current density limiting effect induced by the membrane. However, under the cooler conditions (20^{o}C lower), Segments 3 and 4 increase in current to service the total current required from the stack and heats accordingly. Again, this result highlights

the coupled nature of current and temperature and stresses that both need to be considered to understand performance.

3.3. Transient evolutions during dead-ended anode / purge events at 0.7 A cm^{-2}

Dead-ended anode purge operations have been investigated previously on a similar system where it was proposed that performance transients are due to a combination of pressure, reactant cross-over, reactant consumption and water management issues[37]. However, no insight was available as to the spatiotemporal characteristics.

In this mode of operation the purge valve, located at the fuel exhaust [37,44] is kept closed for an extended time at a constant overall current density of 0.7 A cm^{-2}. This current density was chosen because previous work has highlighted that the voltage decay in dead-ended mode becomes significant over 0.65 A cm^{-2}[37]. Steady-state conditions are attained ~840 s after the purge valve was closed, during which time a significant redistribution of local current occurs, some segments decreasing and others increasing to sustain an overall current constant.

It can be seen from Fig. 9. that as soon as the purge valve is closed, the voltage initially increases by 6 mV; this has been shown to be due to a Nernstian effect caused by the increase in pressure (1 to 1.4 bar absolute) in the anode [37]. After the maximum voltage is attained, it drops with two changes of slope, from 160 $\mu V\ s^{-1}$ to 35 $\mu V\ s^{-1}$ after ~ 360 s, and from 35 $\mu V\ s^{-1}$ to 2 $\mu V\ s^{-1}$ after ~ 840 s. The results from the temperature and current mapping, Fig. 9 and Fig. 8, show that relatively flat temperature and current distribution profiles in through-flow mode have resulted in high gradients in dead-ended mode. Temperature and current density near the inlet

peaks at 0.86 A cm^{-2} and 65 ^{o}C, with low temperature and current density near the exhaust down to 0.42 A cm^{-2} and 35 ^{o}C.

In going from hydrogen through-flow to dead-ended operation, the way that the hydrogen is delivered has fundamentally changed. Although in each case the source of hydrogen has not been limited, in through-flow there is a forced convection supply of hydrogen as it passes through the cell; in dead-ended mode, supply is diffusion driven by the electrochemical consumption of hydrogen[37]. The diffusion of hydrogen is insufficient, and has been shown to suffers from water saturation [38] and flooding along with nitrogen accumulation [42], which produce further hydrogen dilution and worsen diffusion limitations.

Steady state conditions are reached after t >840 s (Fig. 9 a-b), with large spatial electro-thermal gradients across the cell (Fig. 8 c-d), possibly because water condensation cannot reach further areas into the system due to the temperature gradient. As soon as the exhaust valve is opened, the system fully recovers within 240 s, and returns to the conditions prior to the dead-ended period.

In order to avoid possible degradation mechanisms and keep the benefit of dead-ended anode (higher fuel efficiency, low parasitic power consumption), the dead-ended period should be limited to avoid severe gradient formation.

4.Conclusion

For the first time, combined current density and temperature mapping using a single sensor plate has been performed on a polymer electrolyte fuel cell stack to provide a localised electro-thermal performance map. An air-cooled fuel cell is examined that operates in air / hydrogen cross-flow. In the low current density regime, current density distribution is primarily dictated by the anode and hydrogen consumption gradient, with the greatest temperature gradient in the direction of air flow. At high current density regime, temperature starts to drive the current density distribution. The hottest segments reach limiting current densities, attributed to membrane dehydration.

The transient evolution in dead-ended anode mode illustrates local spatiotemporal behaviour, with temporal steady-state condition reached. Understanding the gradients set-up during these transients could be crucial to predict long-term degradation and enhance the system life-time. Such information is particularly valuable for determining where to position discrete thermocouples in practical systems to target and monitor extremes of temperature.

5.Acknowledgements

The authors would like to acknowledge the EPSRC for supporting DB and the Electrochemical Innovation Lab through (EP/G030995/1), (EP/I037024/1) and (EP/J001007/1). We acknowledge the support of Intelligent Energy and UCL for supporting the studentship of QM. PRS acknowledges the Royal Academy of Engineering for Fellowship funding. Financial support by the Austrian Ministry of Transport, Innovation and Technology (BMVIT) and The Austrian Research

Promotion Agency (FFG) is gratefully acknowledged for the funding of the A3FALCON Project.

6.References

[1] Cleghorn SJC, Derouin CR. A printed circuit board approach to measuring current distribution in a fuel cell. J Appl Electrochem 1998;28:663–72.

[2] Brett DJL, Atkins S, Brandon NP, Vesovic V, Vasileiadis N, Kucernak AR. Measurement of the current distribution along a single flow channel of a solid polymer fuel cell. Electrochem Commun 2001;3:628–32.

[3] Brett DJL, Atkins S, Brandon NP, Vasileiadis N, Vesovic V, Kucernak AR. Membrane resistance and current distribution measurements under various operating conditions in a polymer electrolyte fuel cell. J Power Sources 2007;172:2–13. doi:10.1016/j.jpowsour.2007.05.071.

[4] Stumper J, Campbell SA, Wilkinson DP, Johnson MC, Davis M. In-situ methods for the determination of current distributions in PEM fuel cells. Electrochem Acta 1998;43:3773–83.

[5] Kleemann J, Finsterwalder F, Tillmetz W. Characterisation of mechanical behaviour and coupled electrical properties of polymer electrolyte membrane fuel cell gas diffusion layers. J Power Sources 2009;190:92–102. doi:10.1016/j.jpowsour.2008.09.026.

[6] Alaefour I, Karimi G, Jiao K, Shakhshir S Al, Li X. Experimental study on the effect of reactant flow arrangements on the current distribution in proton exchange membrane fuel cells. Electrochim Acta 2011;56:2591–8. doi:10.1016/j.electacta.2010.11.002.

[7] Kirsch S, Hanke-Rauschenbach R, Stein B, Kraume R, Sundmacher K. The Electro-Oxidation of H2, CO in a Model PEM Fuel Cell: Oscillations, Chaos, Pulses. J Electrochem Soc 2013;160:F436–F446. doi:10.1149/2.002306jes.

[8] Alaefour I, Karimi G, Jiao K, Li X. Measurement of current distribution in a proton exchange membrane fuel cell with various flow arrangements – A parametric study. Appl Energy 2012;93:80–9. doi:10.1016/j.apenergy.2011.05.033.

[9] Geske M, Heuer M, Heideck G, Styczynski ZA. Current Density Distribution Mapping in PEM Fuel Cells as An Instrument for Operational Measurements. Energies 2010;3:770–83. doi:10.3390/en3040770.

[10] Büchi FN, Geiger AB, Neto RP. Dependence of current distribution on water management in PEFC of technical size. J Power Sources 2005;145:62–7. doi:10.1016/j.jpowsour.2004.12.039.

[11] Mench MM, Wang CY, Ishikawa M. In Situ Current Distribution Measurements in Polymer Electrolyte Fuel Cells. J Electrochem Soc 2003;150:A1052–A1059. doi:10.1149/1.1584440.

[12] Yu Y, Yuan X-Z, Li H, Gu E, Wang H, Wang G, Pan M. Current mapping of a proton exchange membrane fuel cell with a segmented current collector during the gas starvation and shutdown processes. Int J Hydrogen Energy 2012;37:15288–300. doi:10.1016/j.ijhydene.2012.07.023.

[13] Gerteisen D, Zamel N, Sadeler C, Geiger F, Ludwig V, Hebling C. Effect of operating conditions on current density distribution and high frequency resistance in a segmented PEM fuel cell. Int J Hydrogen Energy 2012;37:7736–44. doi:10.1016/j.ijhydene.2012.02.024.

[14] Gerteisen D, Mérida W, Kurz T, Lupotto P, Schwager M, Hebling C. Spatially Resolved Voltage, Current and Electrochemical Impedance Spectroscopy Measurements. Fuel Cells 2011;11:339–49. doi:10.1002/fuce.201000181.

[15] Hakenjos A, Hebling C. Spatially resolved measurement of PEM fuel cells. J Power Sources 2005;145:307–11. doi:10.1016/j.jpowsour.2005.01.075.

[16] Lottin O, Colinart T, Chupin S, Didierjean S. A multi-instrumented polymer exchange membrane fuel cell□ : Observation of the in-plane non-homogeneities. J Power Sources 2008;180:748–54. doi:10.1016/j.jpowsour.2008.03.002.

[17] Zhang G, Guo L, Ma L, Liu H. Simultaneous measurement of current and temperature distributions in a proton exchange membrane fuel cell. J Power Sources 2010;195:3597–604. doi:10.1016/j.jpowsour.2009.12.016.

[18] Freunberger SA, Schneider IA, Sui P-C, Wokaun A, Djilali N, Büchi FN. Cell Interaction Phenomena in Polymer Electrolyte Fuel Cell Stacks. J Electrochem Soc 2008;155:B704–B714. doi:10.1149/1.2913095.

[19] Santis M, Freunberger SA, Papra M, Wokaun A, Felix NB. Experimental investigation of coupling phenomena in polymer electrolyte fuel cell stacks. J Power Sources 2006;161:1076–83. doi:10.1016/j.jpowsour.2006.06.007.

[20] Hwnag JJ, Chang WR, Peng RG, Chen PY, Su A. Experimental and numerical studies of local current mapping on a PEM fuel cell. Int J Hydrogen Energy 2008;33:5718–27. doi:10.1016/j.ijhydene.2008.07.035.

[21] Gulzow E, Wieser C, Helmbold A. A new technique for two-dimensional current distribution measurements in electrochemical cells. J Appl Electrochem 2000;30:803–7.

[22] Freunberger SA, Reum M, Evertz J, Wokaun A, Büchi FN. Measuring the Current Distribution in PEFCs with Sub-Millimeter Resolution. J Electrochem Soc 2006;153:A2158–A2165. doi:10.1149/1.2345591.

[23] Schneider IA, Dahlen S Von, Wokaun A, Scherer GG. A Segmented Microstructured Flow Field Approach for Submillimeter Resolved Local Current Measurement in Channel and Land Areas of a PEFC. J Electrochem Soc 2010;157:B338–B341. doi:10.1149/1.3274228.

[24] Brett D, Aguiar P, Brandon N, Kucernak A. Measurement and modelling of carbon monoxide poisoning distribution within a polymer electrolyte fuel cell. Int J Hydrogen Energy 2007;32:863–71. doi:10.1016/j.ijhydene.2007.01.019.

[25] Brett DJL, Atkins S, Brandon N, Vesovic V, Vasileiadis N, Kucernak AR. Investigation of reactant transport within a polymer electrolyte fuel cell using localised CO stripping voltammetry and adsorption transients. J Power Sources 2004;133:205–13. doi:10.1016/j.jpowsour.2004.02.007.

[26] Wilkinson M, Blanco M, Gu E, Martin JJ, Wilkinson DP, Zhang JJ, Wang H. In Situ Experimental Technique for Measurement of Temperature and Current Distribution in Proton Exchange Membrane Fuel Cells. Fuel Cell 2006;9:507–11. doi:10.1149/1.2338769.

[27] Matian M, Marquis A, Brett D, Brandon N. An experimentally validated heat transfer model for thermal management design in polymer electrolyte membrane fuel cells. Proc Inst Mech Eng Part A J Power Energy 2010;224:1069–81. doi:10.1243/09576509JPE1011.

[28] Wang M, Guo H, Ma C. Temperature distribution on the MEA surface of a PEMFC with serpentine channel flow bed. J Power Sources 2006;157:181–7. doi:10.1016/j.jpowsour.2005.08.012.

[29] Guo H, Hai M, Ye F, Fang C. Experimental study of temperature distribution on anodic surface of MEA inside a PEMFC with parallel channels flow bed. Int J Hydrogen Energy 2012;37:13155–60. doi:10.1016/j.ijhydene.2012.03.138.

[30] Hakenjos A, Muenter H, Wittstadt U, Hebling C. A PEM fuel cell for combined measurement of current and temperature distribution , and flow field flooding. J Power Sources 2004;131:213–6. doi:10.1016/j.jpowsour.2003.11.081.

[31] Martins LS, Gardolinski JEFC, Vargas JVC, Ordonez JC, Amico SC, Forte MMC. The experimental validation of a simplified PEMFC simulation model for design and optimization purposes. Appl Therm Eng 2009;29:3036–48. doi:10.1016/j.applthermaleng.2009.04.002.

[32] Shimoi R, Masuda M, Fushinobu K, Kozawa Y, Okazaki K. Visualization of the Membrane Temperature Field of a Polymer Electrolyte Fuel Cell. J Energy Resour Technol 2004;126:258–61. doi:10.1115/1.1811119.

[33] Matian M, Marquis AJ, Brandon NP. Application of thermal imaging to validate a heat transfer model for polymer electrolyte fuel cells. Int J Hydrogen Energy 2010;35:12308–16. doi:10.1016/j.ijhydene.2010.08.041.

[34] Brett DJL, Aguiar P, Clague R, Marquis a. J, Schöttl S, Simpson R, Brandon NP. Application of infrared thermal imaging to the study of pellet solid oxide fuel cells. J Power Sources 2007;166:112–9. doi:10.1016/j.jpowsour.2006.12.098.

[35] Jiao K, Alaefour IE, Karimi G, Li X. Simultaneous measurement of current and temperature distributions in a proton exchange membrane fuel cell during cold start processes. Electrochim Acta 2011;56:2967–82. doi:10.1016/j.electacta.2011.01.019.

[36] Meyer Q, Ronaszegi K, Pei-June G, Curnick O, Ashton S, Reisch T, Adcock P, Shearing PR, Brett DJL. Optimisation of air cooled, open-cathode fuel cells: Current of lowest resistance and electro-thermal performance mapping. J Power Sources 2015;291:261–9. doi:10.1016/j.jpowsour.2015.04.101.

[37] Meyer Q, Ashton S, Curnick O, Reisch T, Adcock P, Ronaszegi K, Robinson JB, Brett DJL. Dead-Ended Anode Polymer Electrolyte Fuel Cell Stack Operation Investigated using Electrochemical Impedance Spectroscopy, Off-gas Analysis and Thermal Imaging. J Power Sources 2013;254:1–9. doi:10.1016/j.jpowsour.2013.11.125.

[38] Siegel JB, McKay DA, Stefanopoulou AG, Hussey DS, Jacobson DL. Measurement of Liquid Water Accumulation in a PEMFC with Dead-Ended Anode. J Electrochem Soc 2008;155:B1168–B1178. doi:10.1149/1.2976356.

[39] Sasmito AP, Mujumdar AS. Performance evaluation of a polymer electrolyte fuel cell with a dead-end anode: A computational fluid dynamic study. Int J Hydrogen Energy 2011;36:10917–33. doi:10.1016/j.ijhydene.2011.05.171.

[40] Chen J, Siegel JB, Matsuura T, Stefanopoulou AG. Carbon Corrosion in PEM Fuel Cell Dead-Ended Anode Operations. J Electrochem Soc 2011;158:B1164–B1174. doi:10.1149/1.3609770.

[41] Chen J, Siegel JB, Stefanopoulou AG, Waldecker JR. Optimization of purge cycle for dead-ended anode fuel cell operation. Int J Hydrogen Energy 2013;38:5092–105. doi:10.1016/j.ijhydene.2013.02.022.

[42] Siegel JB, Bohac S V., Stefanopoulou AG, Yesilyurt S. Nitrogen Front Evolution in Purged Polymer Electrolyte Membrane Fuel Cell with Dead-Ended Anode. J Electrochem Soc 2010;157:B1081–B1093. doi:10.1149/1.3425743.

[43] Muller E, Kolb F, Guzzella L, Stefanopoulou AG, McKay D. Correlating Nitrogen Accumulation With Temporal Fuel Cell Performance. J Fuel Cell Sci Technol 2010;7:1–11.

[44] Noorkami M, Robinson JB, Meyer Q, Obeisun OA, Fraga ES, Reisch T, Shearing PR, Brett DJL. Effect of temperature uncertainty on polymer electrolyte fuel cell performance5. Int J Hydrogen Energy 2014;39:1439–48.

[45] O'Hayre R, Fabian T, Litster S, Prinz FB, Santiago JG. Engineering model of a passive planar air breathing fuel cell cathode. J Power Sources 2007;167:118–29. doi:10.1016/j.jpowsour.2007.01.073.

[46] Rosa DTS, Pinto DG, Silva VS, Silva RA, Rangel CM. High performance PEMFC stack with open-cathode at ambient pressure and temperature conditions. Int J Hydrogen Energy 2007;32:4350–7. doi:10.1016/j.ijhydene.2007.05.042.

[47] Kim B, Lee Y, Woo A, Kim Y. Effects of cathode channel size and operating conditions on the performance of air-blowing PEMFCs. Appl Energy 2013;111:441–8. doi:10.1016/j.apenergy.2013.04.091.

Figure Captions:

Fig. 1 (a) Schematic diagram of the sensor plate, numbered and showing the temperature sensing meanders and shunt resistors at the centre of each segment. (b) This scheme describes how the

current and temperature are measured with shunt resistors and copper meanders. (c) Schematic diagram of the sensor plate inserted in the stack

Fig. 2. Fuel and oxidant flow orientations over the sensor plate. Air flow is from top row (Segments 1-4) to bottom row (Segments 13-16) and hydrogen is from left column (Segments 1-13) to right column (Segments 4-16).

Fig. 3. (a) Evolution of the voltage and temperature, using thermal imaging, vs. current. (b) Thermogram of the air inlet and air exhaust at 0.92 A cm^{-2} and 0.43 A cm^{-2}. Note that the vertical bars represent tie-rods.

Fig.4. Current and temperature distribution from 0 to 0.46 A cm^{-2}. (a) Polarisation curves for current collection segments. (b) Local current density profile at 0.46 A cm^{-2}. (c) Local temperature distribution.

(d) Local temperature profile at 0.46 A cm^{-2}. $\lambda_{O_2} = 40 : \lambda_{H_2} = 4$. Note that hydrogen and air are in cross-flow, the hydrogen flowing from left to right and air from top to bottom, as displayed in Fig. 2.

Fig. 5. Current and temperature distribution from 0.46 to 0.93 A cm^{-2}. (a) Polarisation curves for current collection segments. (b) Local current density profile at 0.93 A cm^{-2}. (c) Local temperature distribution. (d) Local temperature profile at 0.93 A cm^{-2}. $\lambda_{O_2} = 20 : \lambda_{H_2} = 2$. Note that hydrogen and air are in cross-flow, the hydrogen flowing from left to right and air from top to bottom, as displayed in Fig. 2.

Fig. 6. Current and temperature distribution from 0.46 to 0.93 A cm^{-2} of Segments 3 and 4 (low temperature region) and Segments 10 and 14 (high temperature region) (a) Polarisation curves for current collection segments. (b) Temperature distribution as function of current.

Fig. 7. Effect of the dead-ended event during 1440 s. Evolution of the cell voltage, localised current density (a) and temperature transients (b) during a through-flow (TF) and dead-ended anode (DEA) transient at 0.7 A cm^{-2}. $\lambda_{O_2} = 47.14$. $\lambda_{H_2} = 2.8$.

Fig. 8. Current and temperature at 0.7 A cm^{-2} at t = 0 s in through-flow mode (a-b) and t = 840 s in dead-ended mode (c-d).

Graphical Abstract (for review)

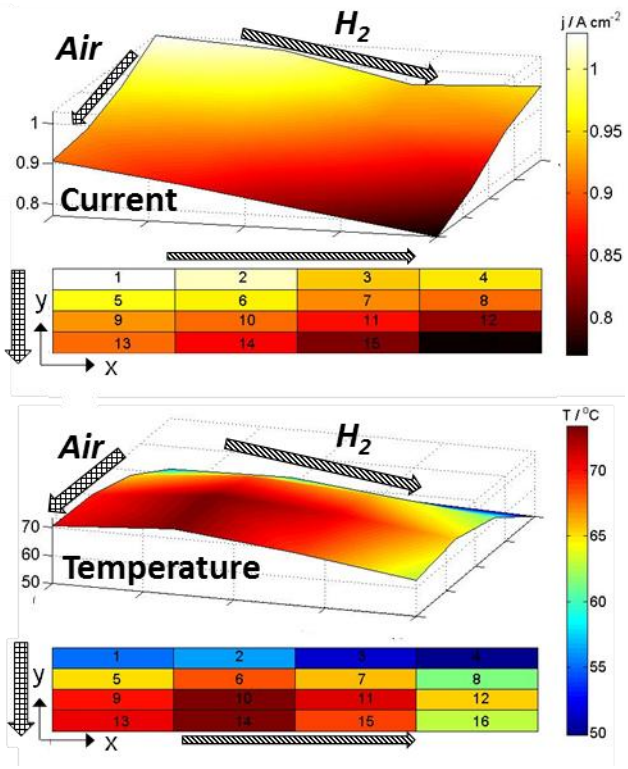

***Highlights (for review)**

- Combined current and temperature mapping as a novel performance metric.
- Large current and temperature gradients form in dead-ended mode.
- Localised extreme temperatures can change the current density gradients.

Combined Current and Temperature Mapping in an Air-Cooled, Open-Cathode Polymer Electrolyte Fuel Cell Under Steady-State and Dynamic Conditions.

Q. Meyer[1], K. Ronaszegi[1], J.B. Robinson[1], M. Noorkami[1], O. Curnick[2], S. Ashton[2], A. Danelyan[2], T. Reisch[2], P. Adcock[2], R. Kraume[3], P. R. Shearing[1], D. J. L. Brett[1]*

[1] Electrochemical Innovation Lab, Department of Chemical Engineering, UCL, London, WC1E 7JE, United Kingdom

[2] Intelligent Energy, Charnwood Building Holywell Park, Ashby Road, Loughborough Leicestershire, LE11 3GB, United Kingdom

[3] S^{++} Simulation Services, Waldstraße 5, 82418 Murnau-Westried, Germany

* Author to whom correspondence should be addressed

Tel.: +44(0)20 7679 3310

Web: www.ucl.ac.uk/electrochemical-innovation-lab

Email: d.brett@ucl.ac.uk

Abstract

In situ diagnostic techniques provide a means of understanding the internal workings of fuel cells so that improved designs and operating regimes can be identified. Here, for the first time, a combined current density and temperature distributed measurement system is used to generate an electro-thermal performance map of an air-cooled, air-breathing polymer electrolyte fuel cell stack operating in an air / hydrogen cross-flow configuration. Analysis is performed in low- and high-current regimes and a complex relationship between localised current density, temperature and reactant supply is identified that describes the way in which the system enters limiting performance conditions. Spatiotemporal analysis was carried out to characterise transient operations in dead-ended anode / purge mode which revealed extensive current density and temperature gradients.

Keywords

Current mapping; temperature mapping; air-breathing fuel cell; performance optimisation; spatiotemporal electro-thermal analysis.

1. Introduction

Polymer electrolyte fuel cells (PEFCs) are complex devices, due to the variety of operational strategies (liquid/air cooled, humidified/dry gases), designs (closed/open cathode, through-flow/dead-ended) and materials. Understanding of the *in-situ* behaviour and more specifically of the complex interaction between localised current and temperature is crucial for the development of improved systems.

Current mapping was first introduced by Cleghorn and Derouin[1] and Brett *et al.* [2,3], using printed circuit board (PCB) technology to produce segmented current collector plates, along with Stumper *et al.*[4], using segmented membranes. This technique shows that significant current density gradients can be generated as a result of fuel and oxidant depletion. Other techniques have proven the value of localised current measurements, including segmented PCBs [1,3,5–9], segmented current collector plates [10–12], shunt resistors [13–15] and Hall effect sensors [16–21]. Measurements have also been performed at sub-millimetre resolution [22,23], investigating the gradients across the land and channel areas. Most studies highlighted uneven performance under high current density, uneven fuel consumptions [2,5,6,14], the crucial influence of the operating conditions [3,13,19], stoichiometric ratios [8,11,12,20], fuel orientations [6,13], water management [10], CO electro-oxidation [7] and CO poisoning [24,25] distribution.

Temperature distribution has also been extensively studied, identifying areas of higher electrochemical activity, hot spot formation and fuel depletion. Thermocouples can provide a crude measure of temperature inside fuel cells [16,17,26,27] but have accuracy limited to $\pm 1^{o}C$ and cannot provide high spatial resolution. Moreover, thermocouples need to be inserted inside the fuel cell, which often requires design modifications. In contrast, infrared thermal imaging can provide very high spatial and temperature resolution [28–34], yet it typically requires use of specially designed fuel cells with a window transparent to infrared radiation, or is otherwise confined to measurement of the outer surface of a cell or stack.

Although current density and temperature have been separately investigated, little has been reported on the combined current and temperature mapping of PEFCs. Studies have used micro-thermocouples arrays inserted within a cell [17,35] and infrared transparent windows [15,30] for temperature measurement; current density measurements performed using PCB segment plates. In the case of the thermocouple insertion method [17,35], they have to be positioned between the cathode flow field and the membrane electrode assembly (MEA) to provide accurate reading, which could affect the flow of reactants and access to the electrodes; similarly, the introduction of the window [15,30] might alter the water condensation, and overall thermal management aspects of cell performance.

Comprehensive understanding of temperature and current density distribution is essential for effective design of PEFCs to assess steady-state operation over a range of operating conditions / modes. For air-cooled open-cathode systems, in which a stream of air generated by external fans concurrently services both the cooling requirement of the stack and supply of oxygen to the cathode, the need to understand the link between electrochemical and thermal performance is particularly important. The electro-thermal performance of such systems has been investigated previously at a whole-stack level[36], but methods of spatiotemporal electro-thermal analysis are required.

Knowledge of the temperature and current density distribution is also essential for understanding transient processes occurring in PEFCs operated in dead-ended mode. During the voltage decay observed in dead-ended mode [37–41], multiple processes are have been identified to play a part, including water accumulation

(highlighted using neutron imaging [37,38]) and nitrogen accumulation (measured via off-gas analysis [37,42,43]).

Meyer *et al*. [37] reported an increase of the overall temperature and ohmic resistance in dead-ended mode. Eventually, local current density could be much higher than the average, and the overall effect could be a local drying of the membrane due to the enhanced reaction heat. Therefore, understanding of the spatiotemporal evolution of the electro-thermal map at constant load but in dead-ended mode would be useful to investigate these claims.

Here, we present the results obtained using a PCB sensor plate device that incorporates both current collection and temperature measurement in close registration with each other. The technique is applied to an air-cooled PEFC where the plate is inserted at the middle of a 5-cell stack. Both steady-state and dynamic operation are investigated.

2. Experimental

Fuel cell testing - A 5-cell (60 cm^2 active area) air-cooled fuel cell stack was used for testing (Intelligent Energy Ltd., UK). The membrane electrode assembly was composed of commercially available gas diffusion layers and commercially available state-of-the art membrane with Pt loading of 0.1 and 0.4 mg cm^{-2} on the anode and cathode, respectively.

The fuel cell test station supplied dry, non-heated, hydrogen (with a purity of 99.995 %) into the anodes and air was blown by three fans (SanAce 36, Sanyo Denki) to the

open-cathode channels. The exhaust hydrogen flow rate in through-flow mode was measured using a thermal mass flow meter (MassVIEW, Bronkhorst) to be 4.7 SLPM (standard litres per minute) when no load was applied. The fans, which provide cooling and air supply to the cathode, were controlled by a programmable power supply (3649A Agilent). The current drawn from the PEFC was controlled by an electronic load (6060B, Agilent) in galvanostatic mode. An in-house computer controlled system coordinates the air, hydrogen, cooling and electrical valves (LabVIEW, National Instruments) as well as recording and presenting data using a data acquisition card (PCI 6221, National Instruments). Ambient temperature, pressure (absolute) and relative humidity (RH) were measured, being of around 25 °C, 1.02 bar (Abs) and 40% RH respectively, during all tests. The operation of this fuel cell in terms of cathode design, cooling and active channels[36], temperature uncertainty [44] and water management in dead-ended anode mode [37] has been described in previous work.

Surface temperature mapping: Thermal imaging was performed using a 640×512 focal plane array camera (SC5600MB FLIR, UK). The images were recorded using commercially available software (ResearchIR, FLIR ATC, Croissy-Beaubourg, France). The camera has an extended wavelength detector allowing detection of infrared light within the range 2.5 μm - 7 μm. The cavity nature of the cooling and active channels approximate to quasi-blackbody emitters, with an emissivity of 1. The thermal camera used during the experiments has a noise equivalent temperature difference (NETD), a measure of the signal-to-noise ratio, of approximately 19 mK which is within the range of calibration required for the

accurate measurement of absolute temperatures. The geometry of the systems imaged resulted in a pixel resolution of approximately 27 µm across the image.

Combined current and temperature mapping: A device for the measurement of the current and temperature distribution, based on PCB technology, was developed by S++ (S++ Simulation Services, Germany). The device is shown in Fig.2 a. The temperature measurement is made with copper 'meanders'. Copper has a temperature coefficient of resistance of 3.9×10^{-3} K^{-1}. The copper wires are supplied with a constant current of 2 mA and the voltage drop across each wire is measured, with its changes proportional to the temperature variations. Current measurement is made with integrated shunt resistors, using a special alloy with a much lower temperature coefficient than copper, therefore relatively insensitive to temperature changes. The resistance of an individual shunt resistor is ≈ 4 mΩ. The shunt resistors and copper 'meanders' are integrated into a printed circuit board (PCB) with gold plated contact segments. Each rectangular contact segment, reading one current and covering one copper meander has an area of 3.75 cm^2. The 16 segments (Fig. 1 a) combined cover the total membrane active area. A multiplexer successively scans the 16 segments and sends the signal to an amplifier and analog-to-digital converter (Fig. 1 b). Finally, the signal is sent to the computer via a USB interface. After calibration, the actual current density and temperature profile is obtained. The fuel cell is operated in galvanostatic mode, and since isopotential conditions are assumed, an applied total current provides a constant voltage through the plate and a distribution of local current density.

Insertion of the sensor plate into the fuel cell: The sensor plate is integrated between an anode and a cathode plate, in the centre of the fuel cell stack. The air flows through the active and cooling channels (Fig. 1 c) of the stack.

The sensor plate captures the local temperature and current density from the air inlet, from Segments 1, 2, 3, 4, to the air exhaust in Segments 13, 14, 15, 16, and the hydrogen inlet, Segments 1, 5, 9, 13 to hydrogen outlet, Segments 4, 8, 12, 16, as displayed Fig. 2. This flow orientation was be used throughout the work, unless stated otherwise.

3. Results and Discussion

In characterising the electro-thermal performance of the stack, the external temperature distribution is first described using infrared thermal imaging. Then the link between internal temperature and current density distribution is considered under steady-state conditions. Finally, the spatiotemporal electro-thermal performance is examined for dead-ended / purge anode transients.

3.1. Thermal imaging of external stack temperature

The influence of temperature on the performance of air-cooled open-cathode fuel cells has been reported previously using thermal imaging and thermocouples [36,37,44]. However, thermal imaging only gives an indication of the external temperature of the stack and thermocouples are normally limited to a few single-point measurements.

However, when used in combination with an array of internal temperature measurements, thermal imaging provides a useful external boundary condition with very high spatial resolution. By changing the fans' orientations, (either blowing air or aspirating air through the stack), it is possible the capture the temperature of the air inlet or the air outlet.

Fig. 3(a) describes the temperature range and distribution observed on the air inlet and outlet of the stack operating over a range of average current densities. Little influence of the fans' orientations is seen on the voltage response.

The temperature distribution over the x-axis, for the air inlet and air exhaust, is depicted using bars centred at the average temperature in Fig. 5(a). The temperature span is quite significant over the x-axis and increases with higher current densities up to 17 ^{o}C at 0.92 A cm^{-2}. It also significantly increases over the y-axis, with a temperature span reaching 30 ^{o}C at limiting current density.

Thermograms in Fig. 2 (b) reveal hot spots towards the hydrogen inlet (left) of the stack, however, the ability to determine the cause of this localised heating effect is limited. Thermal imaging only provides the surface temperature; in order to obtain the heat profile inside the stack, and associate this with current density distribution, a combined internal current and temperature mapping approach is required. Here, such an approach is taken to study steady-state performance in cross-flow configuration and in dynamic mode to investigate dead-end / purge operation.

3.2. Current and temperature mapping

Combined current and temperature distribution mapping was performed in two regimes of operation based on 'low' (<0.46 A cm^{-2}) and 'high' average current density (0.46 to 0.93 A cm^{-2}).

3.2.1. Current and temperature mapping in the low current density regime.

Considering the current density distribution (Fig.4 a and b), one can see that the segments exhibit a gradient along the x-axis (hydrogen flow direction), with decreasing current density the further away from the hydrogen inlet. This is consistent with the consumption, and depletion, of hydrogen, even though the hydrogen has a stoichiometry of λ_{H2} = 4. The oxygen stoichiometry, based on a constant air flow rate, generated by the fans through the tests (details on the calculations can be found in previous work[36]) is of 40 at 0.46 A cm^{-2}. In the y-axis (air flow direction) it can be seen that there is a change in direction of gradient at the start and end of the cell. The columns on the left (at the hydrogen inlet) actually increase in current, whereas those at the hydrogen exit decrease in the air flow direction.

The temperature increases approximately linearly with increasing current density in every segment (Fig.4 c). Although the current density is similar in the first and second column, the first column remains slightly colder because it is fed with hydrogen at ambient temperature, which acts to cool the entrance to the stack. The current density gradient creates a temperature gradient along the x-axis, as a lower current density reduces heat generation (Fig.4 c-d).

The highest temperature is observed around Segments 9, 10, 13, 14 due to the proximity to the hydrogen inlet and air exhaust, this is consistent with the thermal

imaging observations at 0.46 A cm^{-2}, showing the appearance of a hot spot between the first and second quadrant (Fig. 3 b).

This is an example of the coupled effect of current and temperature. The higher temperature at the hydrogen inlet produces a better performance environment with higher electrolyte conductivity, actually leading to improved performance despite the cathode suffering from uneven cooling. Segments 3 and 4 have low temperature and current density, due to the low hydrogen efficiency and proximity to air inlet.

3.2.2. Current and temperature mapping in the high current density regime

Above 0.8 A cm^{-2}, a redistribution of the current distribution profile is observed (Fig. 5 a-b), with substantial current density gradients occurring in both the x- and y-axis. The temperature of most segments (Fig. 5 c-d) increases in an exponential fashion, as a result of the increase in current density.

To focus on performance at high current, Fig. 6 compares segments located at extreme locations of the cell. The current density of Segments 10 and 14, representing the high temperature region, shows that the rate of current increase is tapered, whereas that of Segments 3 and 4, the low temperature region, increases more rapidly with increasing load (Fig. 6 a).

The high temperature region is in excess of 70°C in Segments 13 and 14 (Fig. 6 b); given the very high flow rate and un-humidified air stream, the membrane resistance is likely to increase due to dehydration under these conditions [45–47]. This is a high current density limiting effect induced by the membrane. However, under the cooler conditions (20^{o}C lower), Segments 3 and 4 increase in current to service the total current required from the stack and heats accordingly. Again, this result highlights

the coupled nature of current and temperature and stresses that both need to be considered to understand performance.

3.3. Transient evolutions during dead-ended anode / purge events at 0.7 A cm^{-2}

Dead-ended anode purge operations have been investigated previously on a similar system where it was proposed that performance transients are due to a combination of pressure, reactant cross-over, reactant consumption and water management issues[37]. However, no insight was available as to the spatiotemporal characteristics.

In this mode of operation the purge valve, located at the fuel exhaust [37,44] is kept closed for an extended time at a constant overall current density of 0.7 A cm^{-2}. This current density was chosen because previous work has highlighted that the voltage decay in dead-ended mode becomes significant over 0.65 A cm^{-2}[37]. Steady-state conditions are attained ~840 s after the purge valve was closed, during which time a significant redistribution of local current occurs, some segments decreasing and others increasing to sustain an overall current constant.

It can be seen from Fig. 9. that as soon as the purge valve is closed, the voltage initially increases by 6 mV; this has been shown to be due to a Nernstian effect caused by the increase in pressure (1 to 1.4 bar absolute) in the anode [37]. After the maximum voltage is attained, it drops with two changes of slope, from 160 $\mu V\ s^{-1}$ to 35 $\mu V\ s^{-1}$ after ~ 360 s, and from 35 $\mu V\ s^{-1}$ to 2 $\mu V\ s^{-1}$ after ~ 840 s. The results from the temperature and current mapping, Fig. 9 and Fig. 8, show that relatively flat temperature and current distribution profiles in through-flow mode have resulted in high gradients in dead-ended mode. Temperature and current density near the inlet

peaks at 0.86 A cm^{-2} and 65 ^{o}C, with low temperature and current density near the exhaust down to 0.42 A cm^{-2} and 35 ^{o}C.

In going from hydrogen through-flow to dead-ended operation, the way that the hydrogen is delivered has fundamentally changed. Although in each case the source of hydrogen has not been limited, in through-flow there is a forced convection supply of hydrogen as it passes through the cell; in dead-ended mode, supply is diffusion driven by the electrochemical consumption of hydrogen[37]. The diffusion of hydrogen is insufficient, and has been shown to suffers from water saturation [38] and flooding along with nitrogen accumulation [42], which produce further hydrogen dilution and worsen diffusion limitations.

Steady state conditions are reached after t >840 s (Fig. 9 a-b), with large spatial electro-thermal gradients across the cell (Fig. 8 c-d), possibly because water condensation cannot reach further areas into the system due to the temperature gradient. As soon as the exhaust valve is opened, the system fully recovers within 240 s, and returns to the conditions prior to the dead-ended period.

In order to avoid possible degradation mechanisms and keep the benefit of dead-ended anode (higher fuel efficiency, low parasitic power consumption), the dead-ended period should be limited to avoid severe gradient formation.

4.Conclusion

For the first time, combined current density and temperature mapping using a single sensor plate has been performed on a polymer electrolyte fuel cell stack to provide a localised electro-thermal performance map. An air-cooled fuel cell is examined that operates in air / hydrogen cross-flow. In the low current density regime, current density distribution is primarily dictated by the anode and hydrogen consumption gradient, with the greatest temperature gradient in the direction of air flow. At high current density regime, temperature starts to drive the current density distribution. The hottest segments reach limiting current densities, attributed to membrane dehydration.

The transient evolution in dead-ended anode mode illustrates local spatiotemporal behaviour, with temporal steady-state condition reached. Understanding the gradients set-up during these transients could be crucial to predict long-term degradation and enhance the system life-time. Such information is particularly valuable for determining where to position discrete thermocouples in practical systems to target and monitor extremes of temperature.

5.Acknowledgements

The authors would like to acknowledge the EPSRC for supporting DB and the Electrochemical Innovation Lab through (EP/G030995/1), (EP/I037024/1) and (EP/J001007/1). We acknowledge the support of Intelligent Energy and UCL for supporting the studentship of QM. PRS acknowledges the Royal Academy of Engineering for Fellowship funding. Financial support by the Austrian Ministry of Transport, Innovation and Technology (BMVIT) and The Austrian Research

Promotion Agency (FFG) is gratefully acknowledged for the funding of the A3FALCON Project.

6.References

[1] Cleghorn SJC, Derouin CR. A printed circuit board approach to measuring current distribution in a fuel cell. J Appl Electrochem 1998;28:663–72.

[2] Brett DJL, Atkins S, Brandon NP, Vesovic V, Vasileiadis N, Kucernak AR. Measurement of the current distribution along a single flow channel of a solid polymer fuel cell. Electrochem Commun 2001;3:628–32.

[3] Brett DJL, Atkins S, Brandon NP, Vasileiadis N, Vesovic V, Kucernak AR. Membrane resistance and current distribution measurements under various operating conditions in a polymer electrolyte fuel cell. J Power Sources 2007;172:2–13. doi:10.1016/j.jpowsour.2007.05.071.

[4] Stumper J, Campbell SA, Wilkinson DP, Johnson MC, Davis M. In-situ methods for the determination of current distributions in PEM fuel cells. Electrochem Acta 1998;43:3773–83.

[5] Kleemann J, Finsterwalder F, Tillmetz W. Characterisation of mechanical behaviour and coupled electrical properties of polymer electrolyte membrane fuel cell gas diffusion layers. J Power Sources 2009;190:92–102. doi:10.1016/j.jpowsour.2008.09.026.

[6] Alaefour I, Karimi G, Jiao K, Shakhshir S Al, Li X. Experimental study on the effect of reactant flow arrangements on the current distribution in proton exchange membrane fuel cells. Electrochim Acta 2011;56:2591–8. doi:10.1016/j.electacta.2010.11.002.

[7] Kirsch S, Hanke-Rauschenbach R, Stein B, Kraume R, Sundmacher K. The Electro-Oxidation of H2, CO in a Model PEM Fuel Cell: Oscillations, Chaos, Pulses. J Electrochem Soc 2013;160:F436–F446. doi:10.1149/2.002306jes.

[8] Alaefour I, Karimi G, Jiao K, Li X. Measurement of current distribution in a proton exchange membrane fuel cell with various flow arrangements – A parametric study. Appl Energy 2012;93:80–9. doi:10.1016/j.apenergy.2011.05.033.

[9] Geske M, Heuer M, Heideck G, Styczynski ZA. Current Density Distribution Mapping in PEM Fuel Cells as An Instrument for Operational Measurements. Energies 2010;3:770–83. doi:10.3390/en3040770.

[10] Büchi FN, Geiger AB, Neto RP. Dependence of current distribution on water management in PEFC of technical size. J Power Sources 2005;145:62–7. doi:10.1016/j.jpowsour.2004.12.039.

[11] Mench MM, Wang CY, Ishikawa M. In Situ Current Distribution Measurements in Polymer Electrolyte Fuel Cells. J Electrochem Soc 2003;150:A1052–A1059. doi:10.1149/1.1584440.

[12] Yu Y, Yuan X-Z, Li H, Gu E, Wang H, Wang G, Pan M. Current mapping of a proton exchange membrane fuel cell with a segmented current collector during the gas starvation and shutdown processes. Int J Hydrogen Energy 2012;37:15288–300. doi:10.1016/j.ijhydene.2012.07.023.

[13] Gerteisen D, Zamel N, Sadeler C, Geiger F, Ludwig V, Hebling C. Effect of operating conditions on current density distribution and high frequency resistance in a segmented PEM fuel cell. Int J Hydrogen Energy 2012;37:7736–44. doi:10.1016/j.ijhydene.2012.02.024.

[14] Gerteisen D, Mérida W, Kurz T, Lupotto P, Schwager M, Hebling C. Spatially Resolved Voltage, Current and Electrochemical Impedance Spectroscopy Measurements. Fuel Cells 2011;11:339–49. doi:10.1002/fuce.201000181.

[15] Hakenjos A, Hebling C. Spatially resolved measurement of PEM fuel cells. J Power Sources 2005;145:307–11. doi:10.1016/j.jpowsour.2005.01.075.

[16] Lottin O, Colinart T, Chupin S, Didierjean S. A multi-instrumented polymer exchange membrane fuel cell□ : Observation of the in-plane non-homogeneities. J Power Sources 2008;180:748–54. doi:10.1016/j.jpowsour.2008.03.002.

[17] Zhang G, Guo L, Ma L, Liu H. Simultaneous measurement of current and temperature distributions in a proton exchange membrane fuel cell. J Power Sources 2010;195:3597–604. doi:10.1016/j.jpowsour.2009.12.016.

[18] Freunberger SA, Schneider IA, Sui P-C, Wokaun A, Djilali N, Büchi FN. Cell Interaction Phenomena in Polymer Electrolyte Fuel Cell Stacks. J Electrochem Soc 2008;155:B704–B714. doi:10.1149/1.2913095.

[19] Santis M, Freunberger SA, Papra M, Wokaun A, Felix NB. Experimental investigation of coupling phenomena in polymer electrolyte fuel cell stacks. J Power Sources 2006;161:1076–83. doi:10.1016/j.jpowsour.2006.06.007.

[20] Hwnag JJ, Chang WR, Peng RG, Chen PY, Su A. Experimental and numerical studies of local current mapping on a PEM fuel cell. Int J Hydrogen Energy 2008;33:5718–27. doi:10.1016/j.ijhydene.2008.07.035.

[21] Gulzow E, Wieser C, Helmbold A. A new technique for two-dimensional current distribution measurements in electrochemical cells. J Appl Electrochem 2000;30:803–7.

[22] Freunberger SA, Reum M, Evertz J, Wokaun A, Büchi FN. Measuring the Current Distribution in PEFCs with Sub-Millimeter Resolution. J Electrochem Soc 2006;153:A2158–A2165. doi:10.1149/1.2345591.

[23] Schneider IA, Dahlen S Von, Wokaun A, Scherer GG. A Segmented Microstructured Flow Field Approach for Submillimeter Resolved Local Current Measurement in Channel and Land Areas of a PEFC. J Electrochem Soc 2010;157:B338–B341. doi:10.1149/1.3274228.

[24] Brett D, Aguiar P, Brandon N, Kucernak A. Measurement and modelling of carbon monoxide poisoning distribution within a polymer electrolyte fuel cell. Int J Hydrogen Energy 2007;32:863–71. doi:10.1016/j.ijhydene.2007.01.019.

[25] Brett DJL, Atkins S, Brandon N, Vesovic V, Vasileiadis N, Kucernak AR. Investigation of reactant transport within a polymer electrolyte fuel cell using localised CO stripping voltammetry and adsorption transients. J Power Sources 2004;133:205–13. doi:10.1016/j.jpowsour.2004.02.007.

[26] Wilkinson M, Blanco M, Gu E, Martin JJ, Wilkinson DP, Zhang JJ, Wang H. In Situ Experimental Technique for Measurement of Temperature and Current Distribution in Proton Exchange Membrane Fuel Cells. Fuel Cell 2006;9:507–11. doi:10.1149/1.2338769.

[27] Matian M, Marquis A, Brett D, Brandon N. An experimentally validated heat transfer model for thermal management design in polymer electrolyte membrane fuel cells. Proc Inst Mech Eng Part A J Power Energy 2010;224:1069–81. doi:10.1243/09576509JPE1011.

[28] Wang M, Guo H, Ma C. Temperature distribution on the MEA surface of a PEMFC with serpentine channel flow bed. J Power Sources 2006;157:181–7. doi:10.1016/j.jpowsour.2005.08.012.

[29] Guo H, Hai M, Ye F, Fang C. Experimental study of temperature distribution on anodic surface of MEA inside a PEMFC with parallel channels flow bed. Int J Hydrogen Energy 2012;37:13155–60. doi:10.1016/j.ijhydene.2012.03.138.

[30] Hakenjos A, Muenter H, Wittstadt U, Hebling C. A PEM fuel cell for combined measurement of current and temperature distribution , and flow field flooding. J Power Sources 2004;131:213–6. doi:10.1016/j.jpowsour.2003.11.081.

[31] Martins LS, Gardolinski JEFC, Vargas JVC, Ordonez JC, Amico SC, Forte MMC. The experimental validation of a simplified PEMFC simulation model for design and optimization purposes. Appl Therm Eng 2009;29:3036–48. doi:10.1016/j.applthermaleng.2009.04.002.

[32] Shimoi R, Masuda M, Fushinobu K, Kozawa Y, Okazaki K. Visualization of the Membrane Temperature Field of a Polymer Electrolyte Fuel Cell. J Energy Resour Technol 2004;126:258–61. doi:10.1115/1.1811119.

[33] Matian M, Marquis AJ, Brandon NP. Application of thermal imaging to validate a heat transfer model for polymer electrolyte fuel cells. Int J Hydrogen Energy 2010;35:12308–16. doi:10.1016/j.ijhydene.2010.08.041.

[34] Brett DJL, Aguiar P, Clague R, Marquis a. J, Schöttl S, Simpson R, Brandon NP. Application of infrared thermal imaging to the study of pellet solid oxide fuel cells. J Power Sources 2007;166:112–9. doi:10.1016/j.jpowsour.2006.12.098.

[35] Jiao K, Alaefour IE, Karimi G, Li X. Simultaneous measurement of current and temperature distributions in a proton exchange membrane fuel cell during cold start processes. Electrochim Acta 2011;56:2967–82. doi:10.1016/j.electacta.2011.01.019.

[36] Meyer Q, Ronaszegi K, Pei-June G, Curnick O, Ashton S, Reisch T, Adcock P, Shearing PR, Brett DJL. Optimisation of air cooled, open-cathode fuel cells: Current of lowest resistance and electro-thermal performance mapping. J Power Sources 2015;291:261–9. doi:10.1016/j.jpowsour.2015.04.101.

[37] Meyer Q, Ashton S, Curnick O, Reisch T, Adcock P, Ronaszegi K, Robinson JB, Brett DJL. Dead-Ended Anode Polymer Electrolyte Fuel Cell Stack Operation Investigated using Electrochemical Impedance Spectroscopy, Off-gas Analysis and Thermal Imaging. J Power Sources 2013;254:1–9. doi:10.1016/j.jpowsour.2013.11.125.

[38] Siegel JB, McKay DA, Stefanopoulou AG, Hussey DS, Jacobson DL. Measurement of Liquid Water Accumulation in a PEMFC with Dead-Ended Anode. J Electrochem Soc 2008;155:B1168–B1178. doi:10.1149/1.2976356.

[39] Sasmito AP, Mujumdar AS. Performance evaluation of a polymer electrolyte fuel cell with a dead-end anode: A computational fluid dynamic study. Int J Hydrogen Energy 2011;36:10917–33. doi:10.1016/j.ijhydene.2011.05.171.

[40] Chen J, Siegel JB, Matsuura T, Stefanopoulou AG. Carbon Corrosion in PEM Fuel Cell Dead-Ended Anode Operations. J Electrochem Soc 2011;158:B1164–B1174. doi:10.1149/1.3609770.

[41] Chen J, Siegel JB, Stefanopoulou AG, Waldecker JR. Optimization of purge cycle for dead-ended anode fuel cell operation. Int J Hydrogen Energy 2013;38:5092–105. doi:10.1016/j.ijhydene.2013.02.022.

[42] Siegel JB, Bohac S V., Stefanopoulou AG, Yesilyurt S. Nitrogen Front Evolution in Purged Polymer Electrolyte Membrane Fuel Cell with Dead-Ended Anode. J Electrochem Soc 2010;157:B1081–B1093. doi:10.1149/1.3425743.

[43] Muller E, Kolb F, Guzzella L, Stefanopoulou AG, McKay D. Correlating Nitrogen Accumulation With Temporal Fuel Cell Performance. J Fuel Cell Sci Technol 2010;7:1–11.

[44] Noorkami M, Robinson JB, Meyer Q, Obeisun OA, Fraga ES, Reisch T, Shearing PR, Brett DJL. Effect of temperature uncertainty on polymer electrolyte fuel cell performance5. Int J Hydrogen Energy 2014;39:1439–48.

[45] O'Hayre R, Fabian T, Litster S, Prinz FB, Santiago JG. Engineering model of a passive planar air breathing fuel cell cathode. J Power Sources 2007;167:118–29. doi:10.1016/j.jpowsour.2007.01.073.

[46] Rosa DTS, Pinto DG, Silva VS, Silva RA, Rangel CM. High performance PEMFC stack with open-cathode at ambient pressure and temperature conditions. Int J Hydrogen Energy 2007;32:4350–7. doi:10.1016/j.ijhydene.2007.05.042.

[47] Kim B, Lee Y, Woo A, Kim Y. Effects of cathode channel size and operating conditions on the performance of air-blowing PEMFCs. Appl Energy 2013;111:441–8. doi:10.1016/j.apenergy.2013.04.091.

Figure Captions:

Fig. 1 (a) Schematic diagram of the sensor plate, numbered and showing the temperature sensing meanders and shunt resistors at the centre of each segment. (b) This scheme describes how the

current and temperature are measured with shunt resistors and copper meanders. (c) Schematic diagram of the sensor plate inserted in the stack

Fig. 2. Fuel and oxidant flow orientations over the sensor plate. Air flow is from top row (Segments 1-4) to bottom row (Segments 13-16) and hydrogen is from left column (Segments 1-13) to right column (Segments 4-16).

Fig. 3. (a) Evolution of the voltage and temperature, using thermal imaging, vs. current. (b) Thermogram of the air inlet and air exhaust at 0.92 A cm^{-2} and 0.43 A cm^{-2}. Note that the vertical bars represent tie-rods.

Fig.4. Current and temperature distribution from 0 to 0.46 A cm^{-2}. (a) Polarisation curves for current collection segments. (b) Local current density profile at 0.46 A cm^{-2}. (c) Local temperature distribution.

(d) Local temperature profile at 0.46 A cm^{-2}. $\lambda_{O_2} = 40 : \lambda_{H_2} = 4$. Note that hydrogen and air are in cross-flow, the hydrogen flowing from left to right and air from top to bottom, as displayed in Fig. 2.

Fig. 5. Current and temperature distribution from 0.46 to 0.93 A cm^{-2}. (a) Polarisation curves for current collection segments. (b) Local current density profile at 0.93 A cm^{-2}. (c) Local temperature distribution. (d) Local temperature profile at 0.93 A cm^{-2}. $\lambda_{O_2} = 20 : \lambda_{H_2} = 2$. Note that hydrogen and air are in cross-flow, the hydrogen flowing from left to right and air from top to bottom, as displayed in Fig. 2.

Fig. 6. Current and temperature distribution from 0.46 to 0.93 A cm^{-2} of Segments 3 and 4 (low temperature region) and Segments 10 and 14 (high temperature region) (a) Polarisation curves for current collection segments. (b) Temperature distribution as function of current.

Fig. 7. Effect of the dead-ended event during 1440 s. Evolution of the cell voltage, localised current density (a) and temperature transients (b) during a through-flow (TF) and dead-ended anode (DEA) transient at 0.7 A cm^{-2}. $\lambda_{O_2} = 47.14$. $\lambda_{H_2} = 2.8$.

Fig. 8. Current and temperature at 0.7 A cm^{-2} at t = 0 s in through-flow mode (a-b) and t = 840 s in dead-ended mode (c-d).

Figure 1

Click here to download Figure(s): Figure 1.docx

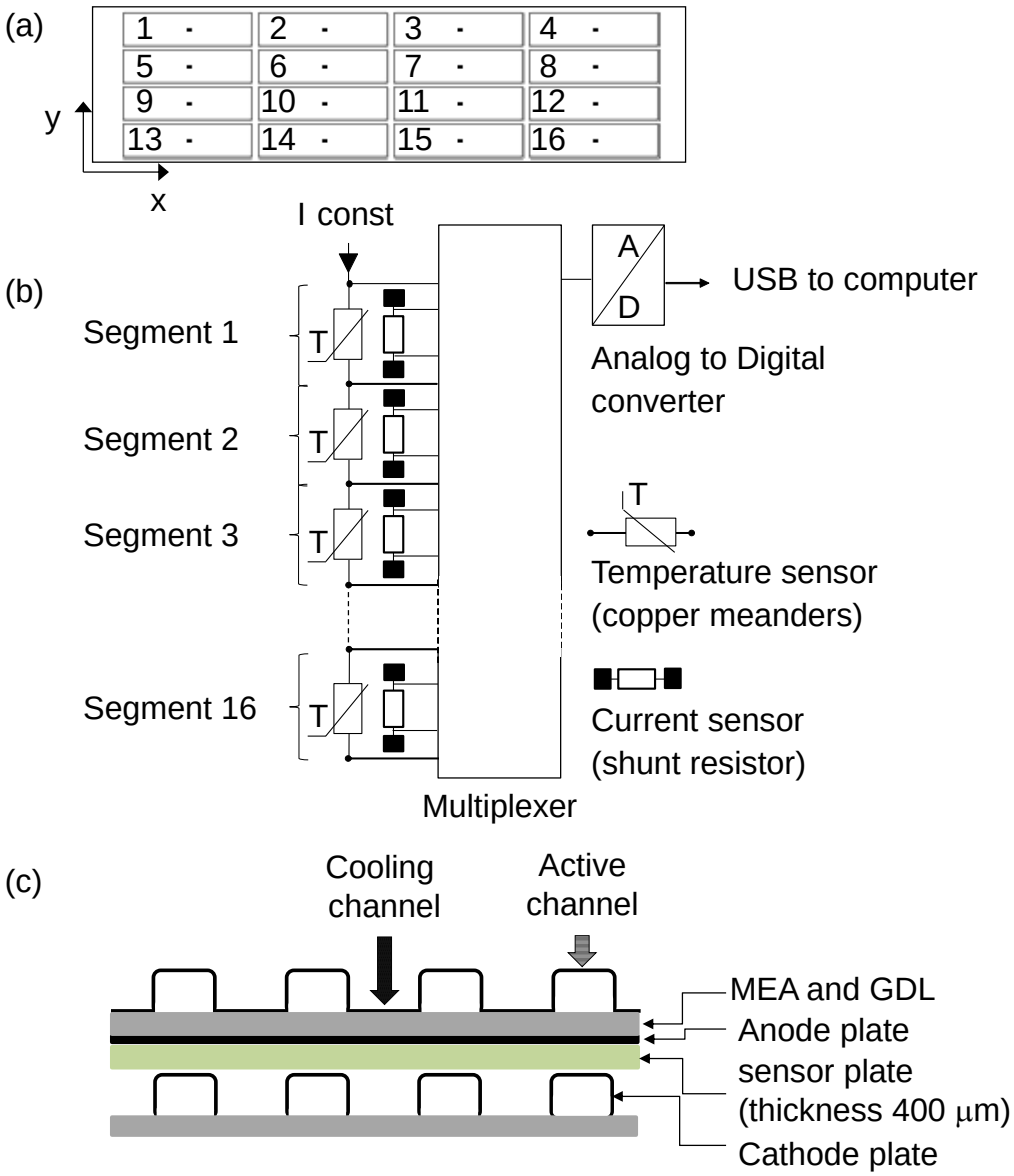

Figure 2

Click here to download Figure(s): Figure 2.docx

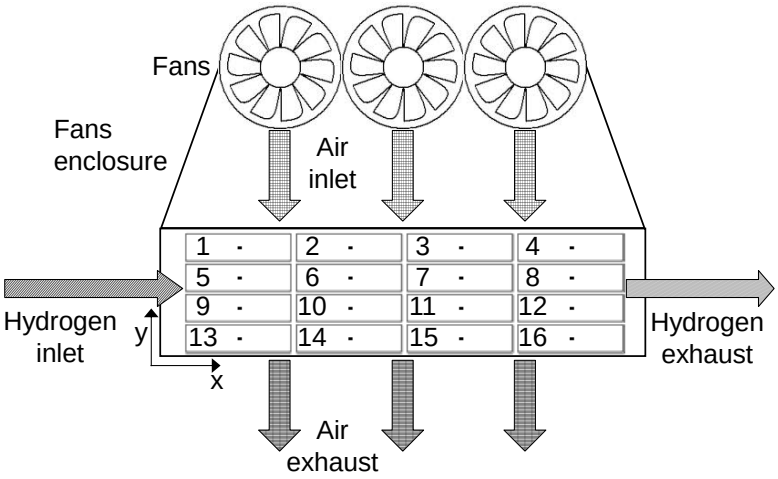

Figure 3

Click here to download Figure(s): Figure 3.docx

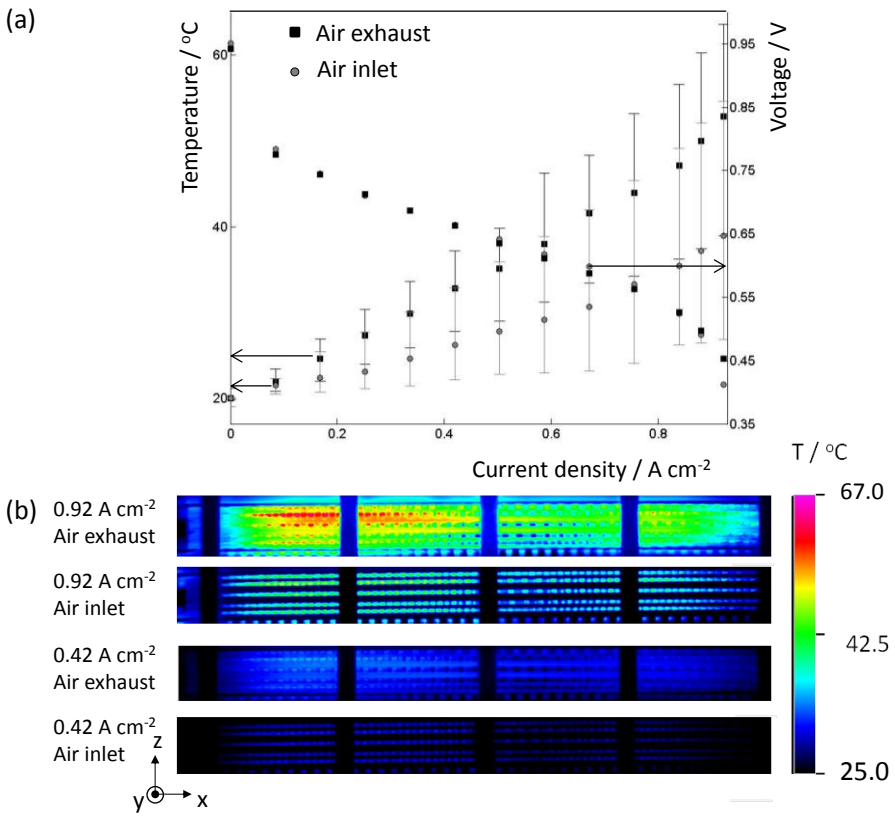

Figure 4

Click here to download Figure(s): Figure 4.docx

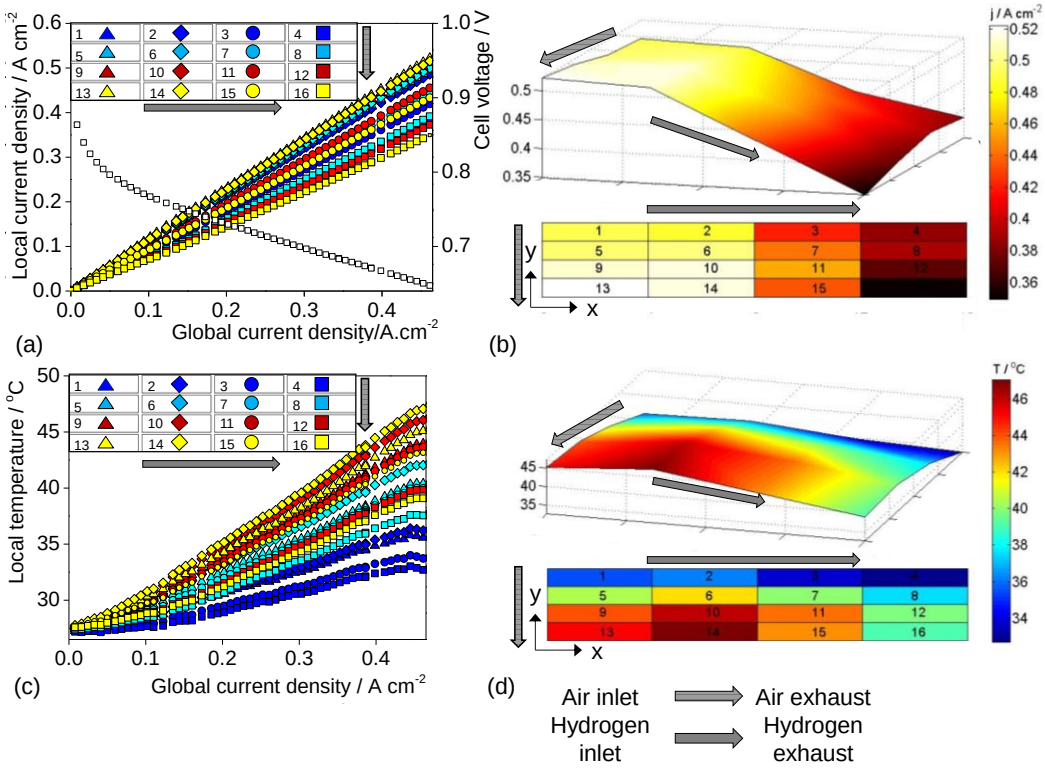

Figure 5

Click here to download Figure(s): Figure 5.docx

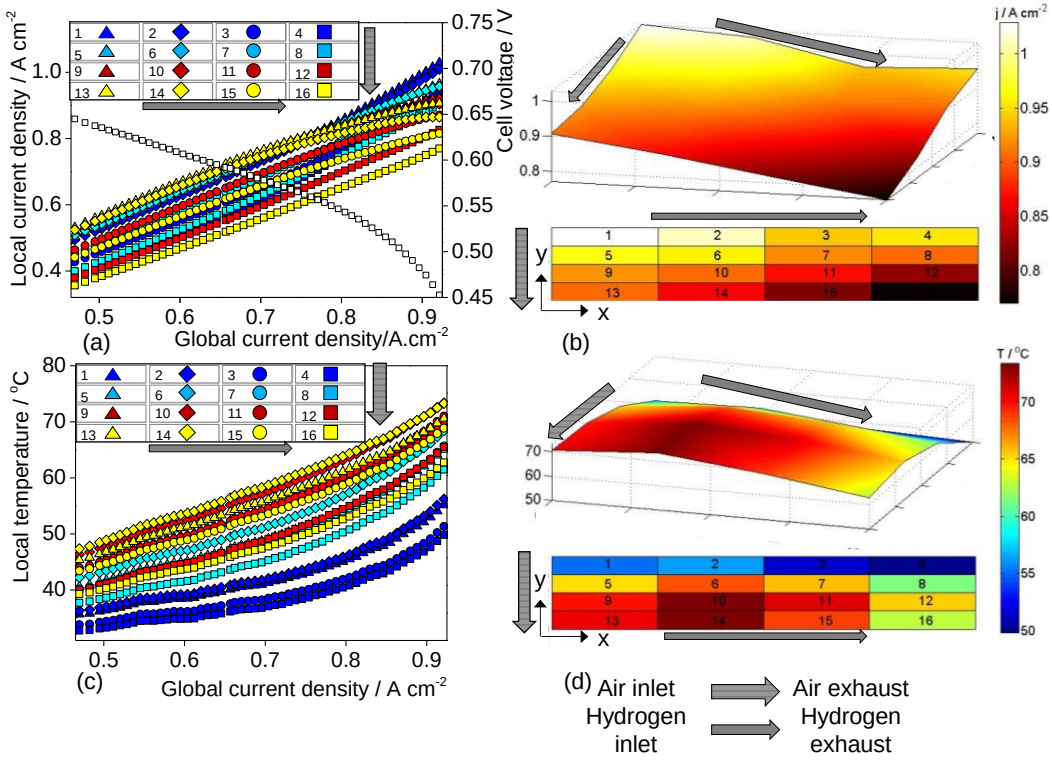

Figure 6

Click here to download Figure(s): Figure 6.docx

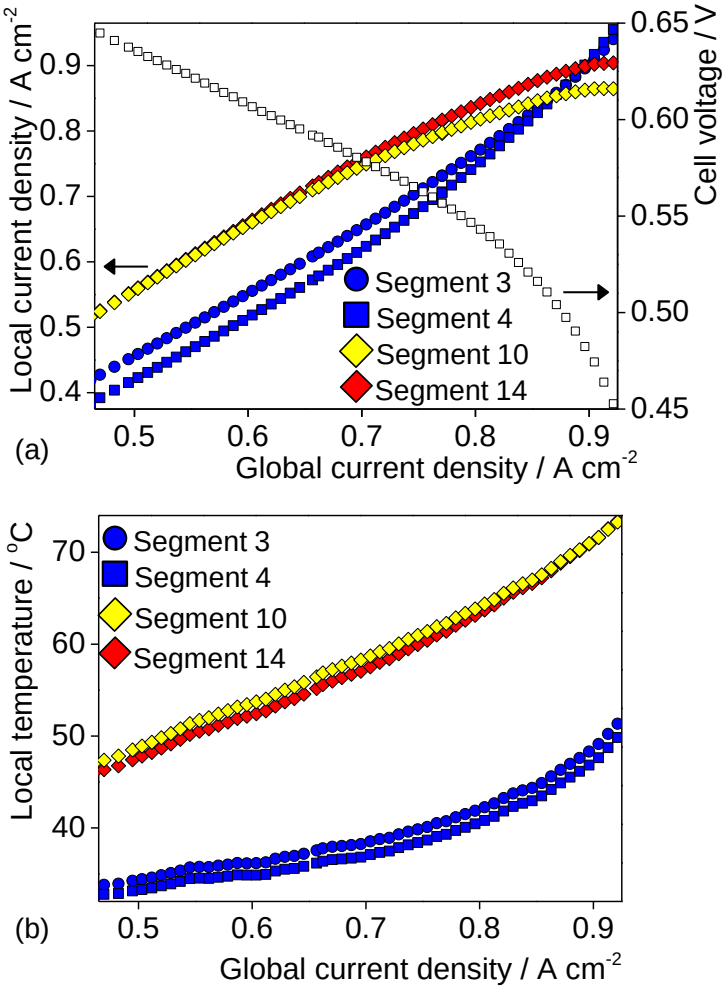

Figure 7

Click here to download Figure(s): Figure 7.docx

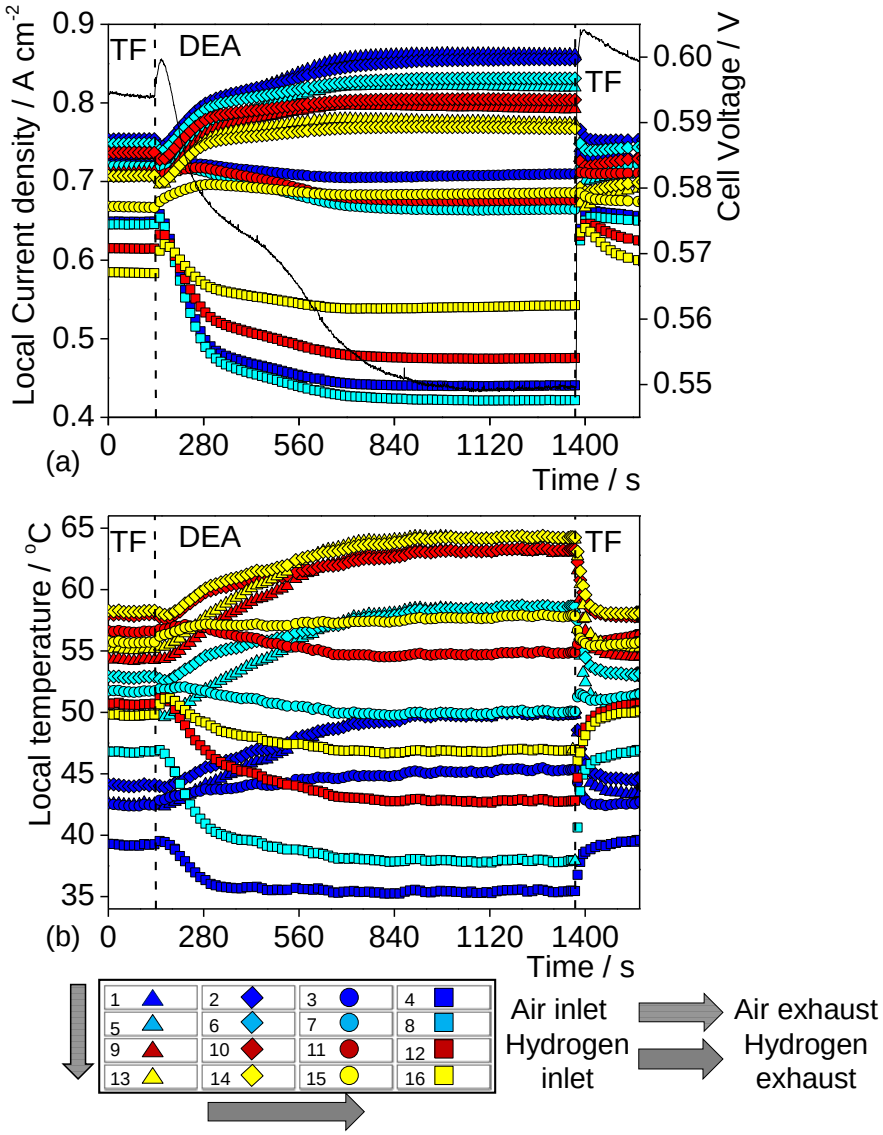

Figure 8

Click here to download Figure(s): Figure 8.docx